Comput Mech (2009) 45:91–107
DOI 10.1007/s00466-009-0417-0

ORIGINAL PAPER

Towards the treatment of boundary conditions for global crack path tracking in three-dimensional brittle fracture

Philippe Jäger · Paul Steinmann · Ellen Kuhl

Received: 24 June 2009 / Accepted: 26 August 2009 / Published online: 27 September 2009

Abstract The aim of the present paper is a systematic elaboration of a three dimensional finite element analysis tool for discontinuous fracture in brittle solids. Brittle or quasi-brittle fracture usually occurs when a material reaches the limit of its strength and no plastic deformation has been observed prior to failure. In the present approach, this kind of failure is characterized by three sets of governing equations: (i) the elastic bulk problem and (ii) the cohesive interface problem regarding the solid deformation field and (iii) the crack tracking problem concerning the crack kinematics. This manuscript describes a unique modular tool set for the coupled set of nonlinear equations. We focus in particular on the boundary conditions for the crack tracking problem of this analysis tool. We critically discuss important implementation details: (i) the choice of crack onset boundary conditions for the additional global field, (ii) the numerical integration, (iii) the modeling of geometrically exact crack tips for cohesive fracture, and (iv) the post-processing procedure for the discontinuity visualization. The potential of the method to simulate brittle fracture is demonstrated by qualitative and quantitative comparisons with experiments from the literature as well as by common benchmark problems.

P. Jäger
Department of Mechanical Engineering, University of Kaiserslautern, 67653 Kaiserslautern, Germany
e-mail: pjaeger@rhrk.uni-kl.de

P. Steinmann (✉)
Department of Mechanical Engineering, Friedrich-Alexander University Erlangen-Nuremberg, 91058 Erlangen, Germany
e-mail: steinmann@ltm.uni-erlangen.de

E. Kuhl
Department of Mechanical Engineering, Stanford University, Stanford, CA 94305, USA
e-mail: ekuhl@stanford.edu

Keywords Discontinuous failure · Brittle fracture · Interface · Cohesive crack concept · Concrete modeling · Visualization

1 Introduction

Brittle or quasi-brittle fracture is characterized by an abrupt collapse of the considered material, or structure. This characteristic behavior takes place when a material reaches the limit of its strength and no plastic deformation can be observed prior to failure. This kind of failure ranges from materials like shattered glasses or ceramics over concrete to faults formed in the crust of the earth. It has recently drawn increasing attention in the context of safety and reliability of concrete buildings, bridges, storage containers, and other engineering structures subjected to high impact loading or explosion. Especially the numerical treatment of tensile dominated brittle fracture of concrete has been under extensive research interest in the past decade, see, e.g., [1–11]. Here, tensile dominated failure refers to degradation phenomena in which the tensile failure patterns can be regarded as dominant over to shear failure which, in turn, is common in metallic materials. As a first approximation to mixed mode failure, fracture parameters for the opening mode I can be used if the shear to tension ratio is moderately small. If shear stress becomes dominant, shear friction and aggregate interlocking can no longer be neglected. Tensile failure of concrete involves progressive microscopic cracking, debonding and other complex irreversible processes of internal damage. The associated softening can coalesce into a discontinuity that separates the material. The discrete crack concept is the approach that reflects these phenomena closest.

Considering this brief description of brittle fracture, it is evident that at least three main building blocks are needed

for the phenomenological numerical modeling of brittle fracture in a truly three dimensional setting. The first building block regards the description of propagating discontinuities in a continuum mechanics finite element setting. The second building block takes into account the softening material response whereas the third building block includes the computation of the fracture propagation direction associated with the geometrical description of the failure surface.

In recent years many promising techniques have been developed to handle the first building block. For the sake of clarity, we would like to classify the following most prominent approaches. The easiest strategies which takes into account real physical crack kinematics, are interface elements, see, e.g., [12–15]. It is evident that this approach is appropriate for situations where the crack path is known a priori whereas for situations where the crack path has to be predicted this approach will obviously produce mesh dependent solutions. An alternative approach which seems to be the most common in industrial applications, is the remeshing technique, see, e.g., [16,17]. The first approach to truly simulate arbitrary discrete failure surfaces in finite element meshes was the embedded discontinuity technique, see, e.g., [18–24]. Motivated by the assumed enhanced strain concept, additional degrees of freedom were introduced locally on the element level to characterize the failure plane. The embedded discontinuity technique convinced through its computational efficiency because the size of the global system of equations was not affected by the new local enhancement.

A further approach which is not based on additional local element degrees of freedom is the extended finite element method XFEM introduced by Belytschko and co-workers, see, e.g., [25,26]. At the additional cost of successively introduced global degrees freedom, smooth discrete cracks could finally be modeled anywhere in the domain, see also [27–30] for two dimensional computations, as well as [31–36] for three dimensional computations. While the XFEM uses the displacement jump as additional global unknown, the method proposed by Hansbo and Hansbo [37–39] works exclusively with deformation degrees of freedom, see also [40–43]. In this manuscript we focus on the latter approach which basically belongs to the category of discontinuous Galerkin methods. However, to round off the approaches valid for the first building block we should mention meshless methods which have also been successfully applied to model arbitrary crack propagation, see, e.g., [44,45].

It should be noted that all these mentioned approaches are discrete in nature: The dissipative softening behavior caused by the fracture process is characterized in terms of surface tractions depending on displacements jumps along the discontinuity surface whereas the bulk material is considered to remain purely elastic. To this end, we use cohesive traction separation laws that constitute the second mentioned building block. The cohesive crack concept has originally been proposed by Dugdale [46] and Barrenblatt [47]. It was further elaborated for concrete materials by Hillerborg [48,49]. The key assumption of the cohesive crack concept is that the introduced crack surfaces are able to transfer stresses within the process zone of the propagating crack. Since the cohesive concept is a very elegant tool to merge all irreversible failure mechanisms into an arbitrary traction separation relation, it has been adopted for the modeling of brittle failure by several authors, see, e.g., [50–55].

Finally we point our attention to the last building block. In a two-dimensional setting, the geometrical description of a crack surface is a line. Tracking the crack is uniquely defined and both the solution and its algorithmic realization are straight forward. Once an element is identified to fail, in the case of brittle fracture typically decided based on a maximum principal stress criterion, the crack extends from a neighboring crack point on the element edge in the direction normal to the principal stress. Hence, this stress based crack propagation criterion always renders a unique and smooth $\mathcal{C}^0$ continuous failure zone in two-dimensional analyses. While the generalization to three dimensions seems to be straightforward on paper, the algorithmic realization requires a number of additional considerations and tool sets that are not required in two-dimensional simulations. This additional complexity has hampered the development of three-dimensional crack propagation algorithms and only few attempts are present in the current literature. In a three-dimensional setting, the element-wise evaluation of local stress-based failure criteria typically generates non-smooth failure surfaces. First attempts have been made to address these issues and a variety of different approaches has been proposed, see, e.g., [7,31–33,35,36]. In the present framework we use the so-called global crack tracking algorithm to ensure a smooth failure surface. This idea was recently introduced by Oliver [56] and has been discussed intensively ever since [57–62]. In this approach, a single level set function is used to describe the failure surface and the scalar values of this level set function are introduced as additional global unknowns which have to be coupled to the fracture problem. In detail, the gradient of the newly introduced scalar-valued field is coupled to the principal stress directions and an additional boundary value problem is solved on the global level. Hence, arbitrarily shaped failure surfaces can be characterized and tracked in a stable and robust manner. With this paper, we would like to share our experience in modeling three-dimensional crack propagation. In particular, we focus on (i) the choice of crack onset boundary conditions for the additional global field, (ii) the numerical integration, (iii) the modeling of geometrically exact crack tips for cohesive fracture, and (iv) the post-processing procedure for the discontinuity visualization. These critical aspects of three-dimensional discrete fracture simulation have been neglected in the literature thus far.

The structure of the paper is as follows: Sect. 1 briefly summarizes the governing equations of the elastic bulk problem, the cohesive interface problem and crack tracking problem including the staggered coupling of these governing equations. In the sequel, Sect. 2 introduces the finite element formulation of the governing equations within a complete nonlinear finite element setting. Additionally some important recommendations and comments about the implementation details are made including the definition and description of different kinds of boundary conditions for the crack tracking problem. In Sect. 3 we present three numerical examples displaying the results which can be obtained with the proposed theoretical and numerical framework. Finally, we conclude the manuscript with a discussion and a brief outlook.

2 Governing equations

The mechanical problem we will describe in this section is essentially governed by three sets of equations: (i) the elastic bulk problem, (ii) the cohesive interface problem, and (iii) the crack tracking problem. The elastic bulk problem and the crack tracking problem are valid in the entire domain $\mathcal{B}$ whereas the cohesive interface problem is valid only on the discontinuity Γ. For the sake of transparency, we restrict the description to one single discontinuity while the extension to multiple discontinuities is straightforward. In this section, we will briefly summarize the corresponding continuous field equations for each of the three building blocks.

2.1 The elastic bulk problem

Let us first characterize the elastic bulk behavior in the body $\mathcal{B}$ which we assume to be crossed by a discontinuity Γ. On each side of this discontinuity, i.e. on $\mathcal{B}^+$ and $\mathcal{B}^-$, we introduce an independent set of deformation maps $\boldsymbol{\varphi}$ which maps particles from their original position $\boldsymbol{X}$ in the reference configuration $\mathcal{B}$ to their current position $\boldsymbol{x}$ in the deformed configuration $\mathcal{S}$ as illustrated in Fig. 1.

$$\boldsymbol{\varphi}(\boldsymbol{X}) := \begin{cases} \boldsymbol{\varphi}^{+}(\boldsymbol{X}) \\ \boldsymbol{\varphi}^{-}(\boldsymbol{X}) \end{cases} \quad F := \begin{cases} \boldsymbol{F}^{+} = \nabla_{\boldsymbol{x}} \boldsymbol{\varphi}^{+} & \forall \boldsymbol{X} \in \mathcal{B}^{+} \\ \boldsymbol{F}^{-} = \nabla_{\boldsymbol{x}} \boldsymbol{\varphi}^{-} & \forall \boldsymbol{X} \in \mathcal{B}^{-} \end{cases} \tag{1}$$

Accordingly, we can introduce independent deformation gradients $\boldsymbol{F}^+$ and $\boldsymbol{F}^-$ and their corresponding Jacobians $J^+ = \det \boldsymbol{F}^+$ and $J^- = \det \boldsymbol{F}^-$ on either side of the discontinuity. In the absence of body forces and inertia terms, the equilibrium equation reduces to the vanishing divergence of the Piola stress $\boldsymbol{P}$ which can be stated independently in both subdomains $\mathcal{B}^+$ and $\mathcal{B}^-$.

$$\operatorname{Div} \boldsymbol{P} = 0 \quad \forall \boldsymbol{X} \in \mathcal{B}^{+} \cup \mathcal{B}^{-} \tag{2}$$

On the external boundary $\partial\mathcal{B}$ which can be subdivided into disjoint parts $\partial\mathcal{B} = \partial\mathcal{B}_u \cup \partial\mathcal{B}_t$ with $\partial\mathcal{B} = \partial\mathcal{B}_u \cap \partial\mathcal{B}_t = \varnothing$ either Dirichlet boundary conditions $\boldsymbol{\varphi} = \boldsymbol{\varphi}^p$ or Neumann boundary conditions $\boldsymbol{P} \cdot \boldsymbol{N} = \boldsymbol{T}^p$ can be prescribed in terms of given deformations $\boldsymbol{\varphi}^p$ or given surface tractions $\boldsymbol{T}^p$. We assume, without loss of generality, a compressible elastic constitutive behavior of Neo-Hookean type inside the bulk. Thus, the Cauchy stress $\boldsymbol{\sigma}$ can be expressed in terms of the Lamé parameters λ and μ. The Cauchy stress $\boldsymbol{\sigma}$ can be related to the Piola stress $\boldsymbol{P}$ through Nanson's formula. In general, these stresses can take different values on both sides of the discontinuity $\mathcal{B}^+$ and $\mathcal{B}^-$.

$$\begin{aligned} \boldsymbol{P} &= J\boldsymbol{\sigma} \cdot \boldsymbol{F}^{-t} \\ \boldsymbol{\sigma} &= \frac{1}{J}\left[\lambda \ln(J)\, \boldsymbol{I} - \mu \boldsymbol{I} + \mu \boldsymbol{F} \cdot \boldsymbol{F}^{t}\right] \quad \forall \boldsymbol{X} \in \mathcal{B}^{+} \cup \mathcal{B}^{-} \end{aligned} \tag{3}$$

What remains for the elastic bulk problem is the initiation of failure. Following the classical principal stress based Rankine criterion, we solve the eigenvalue problem of the Cauchy stress tensor $\boldsymbol{\sigma} = \sum_{i=1}^{3} \lambda_i^{\sigma}\, \boldsymbol{n}_i^{\sigma} \otimes \boldsymbol{n}_i^{\sigma}$ and allow for crack propagation if the largest eigenvalue $\lambda^{\sigma_{\max}}$ exceeds the rupture stress, i.e. $\lambda^{\sigma_{\max}} > \sigma^{crit}$. Furthermore the eigenvector $\boldsymbol{n}_i^{\sigma_{\max}}$, related to the maximal eigenvalue, defines the normal to the crack propagation direction $\boldsymbol{n} = \boldsymbol{n}_i^{\sigma_{\max}}$ in the spatial configuration. The two remaining eigenvectors $\boldsymbol{t}_2 = \boldsymbol{n}_i^{\sigma_2}$ and $\boldsymbol{t}_3 = \boldsymbol{n}_i^{\sigma_3}$ related to the second and the third eigenvector $\lambda^{\sigma_{\max}} > \lambda^{\sigma_2} > \lambda^{\sigma_3}$ span the crack plane in the spatial configuration. Their corresponding material unit vectors $\boldsymbol{T}_2 = \frac{\boldsymbol{F}^{-1}\cdot\boldsymbol{t}_2}{|\boldsymbol{F}^{-1}\cdot\boldsymbol{t}_2|}$ and $\boldsymbol{T}_3 = \frac{\boldsymbol{F}^{-1}\cdot\boldsymbol{t}_3}{|\boldsymbol{F}^{-1}\cdot\boldsymbol{t}_3|}$ will prove essential for the kinematical characterization of the discontinuity surface.

2.2 The cohesive interface problem

In order to generalize our approach we consider all kinds of fracture accompanying microscopic failure mechanism in a phenomenological sense. Hence, we assume that material failure is exclusively attributed to the cohesive interface which is characterized through its own independent set of equations. The introduction of two different deformation fields for both sides of the discontinuity subdomains $\mathcal{B}^+$ and $\mathcal{B}^-$ inherently introduces possible jumps in the deformation map $[\![\boldsymbol{\varphi}]\!] = \boldsymbol{\varphi}^+ - \boldsymbol{\varphi}^- \forall \boldsymbol{X} \in \Gamma$ on the discontinuity.

As illustrated in Fig. 2, all particles initially located on the unique discontinuity surface Γ are mapped onto two surfaces $\overline{\gamma}^+$ and $\overline{\gamma}^-$ in the deformed configuration. To uniquely characterize discontinuous failure at finite deformations, we apply the concept of a fictitious discontinuity $\overline{\boldsymbol{\varphi}}$ which is assumed to be located between the two discontinuity surfaces $\overline{\gamma}^+$ and $\overline{\gamma}^-$ in the deformed configuration, see, e.g., [4,41–43,51].

$$\overline{\boldsymbol{\varphi}} = \frac{1}{2}\left[\boldsymbol{\varphi}^{+} + \boldsymbol{\varphi}^{-}\right] \quad \overline{\boldsymbol{F}} = \frac{1}{2}\left[\boldsymbol{F}^{+} + \boldsymbol{F}^{-}\right] \quad \forall \boldsymbol{X} \in \Gamma \tag{4}$$

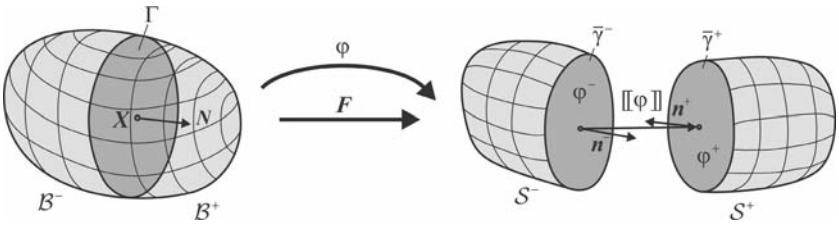

Fig. 1 Elastic bulk problem: independent mappings $\boldsymbol{\varphi}^+$ and $\boldsymbol{\varphi}^-$ on both sides $\mathcal{B}^+$ and $\mathcal{B}^-$ of the discontinuity Γ inherently introduce a jump $[\![\boldsymbol{\varphi}]\!]$ in the deformation field

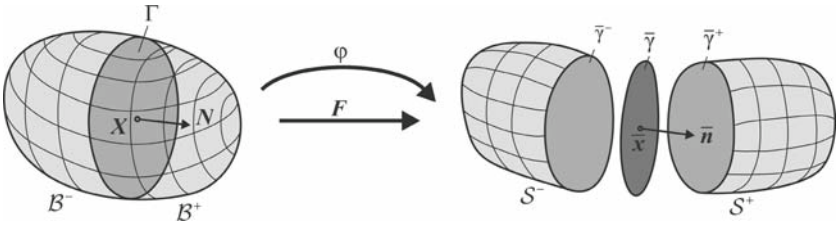

Fig. 2 Cohesive interface problem: concept of fictitious discontinuity surface located between the two discontinuity surfaces $\bar{\gamma}^+$ and $\bar{\gamma}^-$

Again, the corresponding deformation gradient $\overline{\boldsymbol{F}}$ and its Jacobian $J = \det \overline{\boldsymbol{F}}$ follow straightforwardly. The normal $\overline{\boldsymbol{n}}$ to the fictitious discontinuity which will essentially be needed to determine normal and shear resultants on the discontinuity $\overline{\gamma}$ can then be expressed through the classical Nanson formula as $\overline{\boldsymbol{n}} = \overline{J}\,\overline{\boldsymbol{F}}^{-t} \cdot \boldsymbol{N}$. On the internal boundary Γ, i.e. along the fictitious discontinuity, the equilibrium condition

$$\boldsymbol{P}^+ \cdot \boldsymbol{N} = \boldsymbol{P}^- \cdot \boldsymbol{N} = \overline{\boldsymbol{T}} \quad \forall \boldsymbol{X} \in \Gamma \tag{5}$$

states that the cohesive Piola tractions $\overline{\boldsymbol{T}}$ acting on the discontinuity have to be equal in direction and magnitude, however, taking the opposite sign, compare Fig. 2. On the fictitious discontinuity, we apply the cohesive interface concept, for which all inelastic deformation around the crack tip is collectively represented through the cohesive Cauchy tractions $\bar{\boldsymbol{t}}$. Similar to the Cauchy stresses $\boldsymbol{\sigma}$ in the bulk, the cohesive Cauchy tractions $\bar{\boldsymbol{t}}$ on the fictitious discontinuity can be related to the cohesive Piola tractions $\overline{\boldsymbol{T}}$ on the reference domain through Nanson's formula in terms of the area elements da and dA. We conveniently assume a decoupling of the normal and tangential constitutive behavior and introduce the cohesive Cauchy tractions $\bar{\boldsymbol{t}}$ in the following form, see, e.g., [41–43].

$$\begin{aligned} \overline{\boldsymbol{T}} &= \frac{\mathrm{da}}{\mathrm{dA}}\bar{\boldsymbol{t}} \\ \bar{\boldsymbol{t}} &= f_n \exp\left(\frac{f_n}{G_n}[\![\boldsymbol{\varphi}]\!]\cdot\overline{\boldsymbol{n}}\right)\overline{\boldsymbol{n}} + E_t[\boldsymbol{I} - \overline{\boldsymbol{n}}\otimes\overline{\boldsymbol{n}}]\cdot[\![\boldsymbol{\varphi}]\!] \quad \forall \boldsymbol{X} \in \Gamma \end{aligned} \tag{6}$$

In the normal direction, f_n and G_n denote the tensile strength and the fracture energy, respectively. In the tangential direction, E_t denotes the shear stiffness.

2.3 The crack tracking problem

The characterization of smooth three dimensional failure surfaces is handled through a global crack tracking algorithm which introduces an additional set of partial differential equations. The general idea to represent the crack in the form of iso-surfaces $\phi = \text{const}$ of an additionally introduced field $\phi(\boldsymbol{X})$ is relatively novel, [56–62] yet conceptually simple: a particular iso-surface of constant value, e.g., the surface of level zero $\phi = 0$, is chosen to be the kinematical representation of the discrete three-dimensional failure surface. Conceptually speaking, the goal of the crack tracking problem is to find the scalar field $\phi(\boldsymbol{X})$ which is the solution to the following field equation

$$\mathrm{Div}\, \boldsymbol{J} = 0 \quad \forall \boldsymbol{X} \in \mathcal{B} \tag{7}$$

where the flux vector $\boldsymbol{J}$ is a linear function of the gradient of ϕ.

$$\boldsymbol{J} = [\boldsymbol{T}_2 \otimes \boldsymbol{T}_2 + \boldsymbol{T}_3 \otimes \boldsymbol{T}_3] \cdot \nabla_X \phi \qquad \forall \boldsymbol{X} \in \mathcal{B} \tag{8}$$

By construction, the particular format for the anisotropic constitutive tensor $\boldsymbol{D} = \boldsymbol{T}_2 \otimes \boldsymbol{T}_2 + \boldsymbol{T}_3 \otimes \boldsymbol{T}_3$ ensures that the flux $\boldsymbol{J}$ is always a weighted linear combination of the tangent vectors $\boldsymbol{T}_2$ and $\boldsymbol{T}_3$ which as mentioned before are the remaining two eigenvectors of the Rankine criterion in the reference configuration. Since the anisotropy tensor $\boldsymbol{D}$ is rank deficient, we apply slight perturbations ε as $\boldsymbol{D} = \boldsymbol{T}_2 \otimes \boldsymbol{T}_2 + \boldsymbol{T}_3 \otimes \boldsymbol{T}_3 + \varepsilon\, \boldsymbol{I}$ to ensure that the overall system is solvable. The problem of finding $\phi = \text{const.}$ is obviously a classical boundary value problem in terms of the field $\phi(\boldsymbol{X})$ characterized through an anisotropic Laplace equation. On the boundary $\partial\mathcal{B}$ which can be subdivided into disjoint parts $\partial\mathcal{B} = \partial\mathcal{B}_\phi \cup \partial\mathcal{B}_J$ with $\partial\mathcal{B} = \partial\mathcal{B}_\phi \cap \partial\mathcal{B}_J = \varnothing$, either Dirichlet boundary conditions $\phi = \phi^p$ or Neumann boundary conditions $\boldsymbol{J} \cdot \boldsymbol{N} = J^{\mathrm{p}}$ can be prescribed. Typically, we assume a flux-free boundary and apply homogeneous Neumann boundary conditions $\boldsymbol{J} \cdot \boldsymbol{N} = J^{\mathrm{p}} = 0$.

3 Finite element formulation

In this section, we illustrate how we discretize and solve the governing equations (2), (5) and (7) within a nonlinear finite element setting. In addition, we provide some important recommendations and comments about the implementation details. As a basis for the finite element formulation, we reconsider the elastic bulk problem and the cohesive interface problem, which are inherently strongly coupled, compare Fig. 3. Both, however, are only weakly coupled to the crack tracking problem. By this means, we first solve the bulk and interface equilibrium simultaneously and then solve the crack kinematics in a post-processing step.

3.1 Weak form

After multiplication with the corresponding test functions $\delta\boldsymbol{\varphi}$, $[\![\delta\boldsymbol{\varphi}]\!]$ and $\delta\phi$, integration over the domain of interest and consideration of the Neumann boundary conditions $\boldsymbol{P}\cdot\boldsymbol{N}=\boldsymbol{T}^p$ and $\boldsymbol{J}\cdot\boldsymbol{N}=\boldsymbol{J}^{\mathrm{p}}$, the governing equations render the weak form

$$\begin{aligned}
&\int_{\mathcal{B}^+\cup\mathcal{B}^-}\delta\boldsymbol{F}:\boldsymbol{P}\,\mathrm{dV}+\int_{\Gamma}[\![\delta\boldsymbol{\varphi}]\!]\cdot\overline{\boldsymbol{T}}\,\mathrm{dA}=\int_{\partial\mathcal{B}t}\delta\boldsymbol{\varphi}\cdot\boldsymbol{T}^p\mathrm{dA}\\
&\int_{\mathcal{B}}\nabla_X\delta\phi\cdot\boldsymbol{J}\,\mathrm{dV}=\int_{\partial\mathcal{B}_J}\delta\phi\,\boldsymbol{J}^{\mathrm{p}}\,\mathrm{dA}
\end{aligned}\tag{9}$$

in the reference configuration which essentially represent the basis for the discretization to be discussed in the sequel.

3.2 Discretization

For the finite element formulation it proves convenient to distinguish between standard continuous elements and discontinuous elements which are crossed by the discontinuity surface. For the continuous elements we use a standard Bubnov-Galerkin scheme and furthermore we apply a standard isoparametric interpolation of the test functions $\delta\boldsymbol{\varphi}$, the deformation $\boldsymbol{\varphi}$, and their gradients $\delta\boldsymbol{F}$ and $\boldsymbol{F}$. For the discontinuous elements, we apply an independent interpolation of the deformation field $\boldsymbol{\varphi}^+$ and $\boldsymbol{\varphi}^-$ and its gradient $\boldsymbol{F}^+$ and $\boldsymbol{F}^-$ on the individual sides of the discontinuity $\mathcal{B}^+$ and $\mathcal{B}^-$. Strictly speaking, both deformation fields $\boldsymbol{\varphi}^+$ and $\boldsymbol{\varphi}^-$ are interpolated independently over the element. In detail, we essentially double the degrees of freedom of the entire element. The interpolated fields are then set to zero on one side of the discontinuity, while they take their usual values on the other side.

For the crack tracking problem, we again apply a standard linear interpolation of the test and trial functions $\delta\phi$ and ϕ and their gradients $\nabla_X\,\delta\phi$ and $\nabla_X\,\phi$ which leads to the following set of approximations.

$$\begin{aligned}
\delta\boldsymbol{\varphi}&=\textstyle\sum_i\delta\boldsymbol{\varphi}_i N^i & \delta\boldsymbol{F}&=\textstyle\sum_i\delta\boldsymbol{\varphi}_i\otimes\nabla_X N^i\\
\boldsymbol{\varphi}&=\textstyle\sum_j\boldsymbol{\varphi}_j N^j & \boldsymbol{F}&=\textstyle\sum_j\boldsymbol{\varphi}_j\otimes\nabla_X N^j\\
[\![\delta\boldsymbol{\varphi}]\!]&=\textstyle\sum_{\bar{i}}\delta\boldsymbol{\varphi}_{\bar{i}}\overline{N^i} & \delta\overline{\boldsymbol{F}}&=\textstyle\sum_{\bar{i}}\delta\boldsymbol{\varphi}_{\bar{i}}\otimes\nabla_X\overline{N^i}\\
[\![\boldsymbol{\varphi}]\!]&=\textstyle\sum_{\bar{j}}\boldsymbol{\varphi}_{\bar{j}}\overline{N^j} & \overline{\boldsymbol{F}}&=\textstyle\sum_{\bar{j}}\boldsymbol{\varphi}_{\bar{j}}\otimes\nabla_X\overline{N^j}\\
\delta\phi&=\textstyle\sum_i\delta\phi_i N^i & \nabla_X\delta\phi&=\textstyle\sum_i\delta\phi_i\nabla_X N^i\\
\phi&=\textstyle\sum_j\phi_j N^j & \nabla_X\phi&=\textstyle\sum_j\phi_j\nabla_X N^j
\end{aligned}\tag{10}$$

Here N^i and N^j are the standard shape functions for constant strain tetrahedral elements and $i,j=1\ldots n_{en}$ are the four tetrahedral nodes. To unify the notation, we have introduced the sets $\overline{N^{\bar{i}}}$ and $\overline{N^{\bar{j}}}$ which consist of the element shape functions N evaluated on Γ multiplied by the corresponding algebraic sign. The overbars indicate the discontinuous elements, for which we have doubled the degrees of freedom such that $\bar{i},\bar{j}=1\ldots n^+_{en}+n^-_{en}$ are the doubled four, i.e. eight, tetrahedral nodes. Accordingly $\nabla_X\overline{N}$ denotes the gradient of the shape functions N evaluated on the discontinuity Γ, weighted by the factor $\frac{1}{2}$. With the help of the above mentioned discretizations, the weak forms can be cast into the following discrete residual statements.

$$\begin{aligned}
\mathbf{R}^{\varphi}_I&=\mathop{\mathbf{A}}_{e=1}^{n_{el}}\int_{\mathcal{B}_e\cup\mathcal{B}_d^{+,-}}\nabla_X N^i\cdot\boldsymbol{P}\,\mathrm{dV}\\
&\quad+\int_{\overline{\Gamma}}\overline{N^i}\,\overline{\boldsymbol{T}}([\![\delta\boldsymbol{\varphi}]\!])\mathrm{d}\overline{\mathrm{A}}-\int_{\partial\mathcal{B}t_e}N^i\boldsymbol{T}^p\mathrm{dA}=\mathbf{0}\\
\mathrm{R}^{\phi}_I&=\mathop{\mathbf{A}}_{e=1}^{n_{el}}\int_{\mathcal{B}_e}\nabla_X N^i\cdot\boldsymbol{J}\,\mathrm{dV}-\int_{\partial\mathcal{B}_{J_e}}N^i\boldsymbol{J}^{\mathrm{p}}\mathrm{dA}=0
\end{aligned}\tag{11}$$

Thereby, the operator $\mathbf{A}_{e=1}^{n_{el}}$ denotes the assembly of all element contributions including the continuous ones e and the discontinuous ones $d^{+,-}$, respectively. Obviously, the first residual $\mathbf{R}^{\varphi}_I$ is nonlinear in the unknown deformation field $\boldsymbol{\varphi}(\boldsymbol{X})$ whereas the latter residual $\mathrm{R}^{\phi}_I\,\phi(\boldsymbol{X})$ is linear in the unknown field $\phi(\boldsymbol{X})$. Hence, the nonlinear set of Eqs. $(11)_1$ is solved numerically based on an incremental iterative Newton-Raphson scheme with the incremental stiffness matrix $\mathbf{K}^{\varphi}_{IJ}=\partial\mathbf{R}^{\varphi}_I/\partial\boldsymbol{\varphi}_J$. The system matrix of the linear set of Eqs. $(11)_2$ follows accordingly as $\mathrm{K}^{\phi}_{IJ}=\partial\mathrm{R}^{\phi}_I/\partial\phi_J$.

$$\begin{aligned}
\mathbf{K}^{\varphi}_{IJ}&=\mathop{\mathbf{A}}_{e=1}^{n_{el}}\int_{\mathcal{B}_e\cup\mathcal{B}_d^{+,-}}\nabla_X N^i\cdot[\partial_F\boldsymbol{P}]\cdot\nabla_X N^j\,\mathrm{dV}\\
&\quad+\int_{\bar{\Gamma}}\overline{N^i}[\partial_{\overline{F}}\overline{\boldsymbol{T}}]\cdot\nabla_X\bar{N}^j+\overline{N^i}[\partial_{[\![\delta\boldsymbol{\varphi}]\!]}\overline{\boldsymbol{T}}]\overline{N^j}\,\mathrm{d}\overline{\mathrm{A}}\\
\mathrm{K}^{\phi}_{IJ}&=\mathop{\mathbf{A}}_{e=1}^{n_{el}}\int_{\mathcal{B}_e}\nabla_X N^i\cdot[\partial_{\nabla\phi}\boldsymbol{J}]\nabla_X N^j\,\mathrm{dV}
\end{aligned}\tag{12}$$

The solution renders the incremental update of the deformation field $\mathrm{d}\boldsymbol{\varphi}_{\mathrm{J}}=\sum_{I=1}^{n_{np}}\mathbf{K}^{\varphi-1}_{IJ}\mathbf{R}^{\varphi}_I$ and the crack tracking

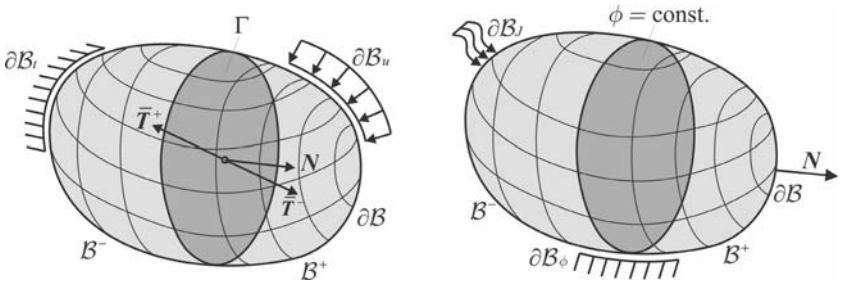

Fig. 3 *Left* elastic bulk and cohesive interface problem. *Right* crack tracking problem

field $\mathrm{d}\phi_J = \sum_{I=1}^{n_{np}} \mathrm{K}_{IJ}^{\phi-1}\mathrm{R}_I^{\phi}$ for all n_{np} nodes. Note that due to the chosen discretization scheme, the number of global node points n_{np} which consists of the standard nodes and the duplicated node points for the discontinuous elements increases progressively during ongoing crack propagation. The terms in brackets, i.e. the fourth, third and second order tensors $[\partial_{\boldsymbol{F}}\boldsymbol{P}]$, $[\partial_{\overline{\boldsymbol{F}}}\overline{\boldsymbol{T}}]$, $[\partial_{[\![\delta\boldsymbol{\varphi}]\!]}\overline{\boldsymbol{T}}]$ and $[\partial_{\nabla\phi}\boldsymbol{J}]$ depend on the choice of the constitutive equations for the stresses $\boldsymbol{P}$ in the continuous body (3), for the tractions $\boldsymbol{T}$ on the discontinuity surface (6) and for the flux $\boldsymbol{J}$ in the domain (8). For the particular choices used in (3) and (6) these linearizations are given, e.g., by Jäger et al. [61]. Since the flux is constant in Eq. (8) with $[\partial_{\nabla\phi}\boldsymbol{J}] = \mathbf{D}$, the crack tracking problem is linear in $\phi(\boldsymbol{X})$ and can thus be solved without further iteration once the nonlinear deformation problem is solved. For the sake of clarity the complete flowchart of the computational algorithm is summarized in Fig. 4.

3.3 Crack extension and crack tip construction

In the presented algorithm the resulting crack tracking field is represented through a level-set function for the description of the crack surface. Without using a detailed mesh independent description of the crack front and by using a linear interpolation of the crack tracking field, the extension of the crack is a planar segment through the entire considered element. It should be noted that this kind of crack surface description can facilitate an inaccurate kinematical description of the emerging failure surface for large elements. However, this kind of discretization error becomes negligible with mesh-refinement. To avoid a crack extension search over the entire set of elements, potentially new crack elements are stored in a list of active crack tip elements. This set of crack tip elements is updated continuously by checking the direct neighbors of the active crack tip elements. Additionally, in order to ensure that the properties of a crack tip are given, not all nodes of the considered element are doubled. Instead, we store the nodes which are part of the free crack tip faces, i.e., the faces without a cracked neighboring element, are used as crack tip front nodes. Additionally, we double only the nodes of the considered element which are not part of this crack tip front nodes. Clearly, this set of crack tip front nodes is also updated continuously during ongoing crack propagation. The resulting displacement field ensures the properties of crack tip which are illustrated in Fig. 5.

Besides, the kinematical description of the crack surface in terms of a scalar valued tracking field might seem cumbersome at first, yet it has some advantages over traditional approaches. It inherently avoids an ill-posedness of the stiffness matrix which is common to traditional approaches if the crack surface strikes the vicinity of a node and the resulting crack surface becomes very small. In the present approach based on a C^0 continuous, scalar valued crack tracking function, however, we control the minimum edge-length of the support of a node, i.e., all element edges connected to the considered node and modify the ϕ value of the considered node. In detail, the nodal value is modified, if the minimal edge length is less than 0.5%, which has turned out to yield reasonable results.

3.4 Splitting of elements and numerical integration

The next important ingredient of the present algorithm concerns the splitting of elements and the numerical integration during the computation of the incremental stiffness matrix $\mathbf{K}_{IJ}^{\varphi}e$ and the element residuals $\mathbf{R}_I^{\varphi}e$ for the discontinuous elements. For these computations it proves convenient to distinguish between the volumetric parts dV and the crack surface parts $\mathrm{d}\overline{\mathrm{A}}$ of the incremental stiffness matrix and the element residuals, compare Eq. (11) and (12) respectively. Furthermore, the geometry of the discontinuous elements can simply be represented by the intersection points in the reference configuration. Hence, the intersection points as well as the crack surface and the volume of the considered elements in the reference configuration do not change during ongoing crack propagation.

In general, two different functions have to be evaluated on both sides of the discontinuous elements for the numerical integration of the volume integrals. The underlying split of a tetrahedral element can produce two different combinations of sub-elements depending on whether the crack surface forms a triangle or a quadrilateral, see in detail, e.g., [4,35,42,43,60]. In the former case, we obtain a four-node tetrahedron and a six-node wedge element, whereas in the latter case we obtain two six-node wedge elements. In contrast to the literature [35,42,43], where the wedge element is

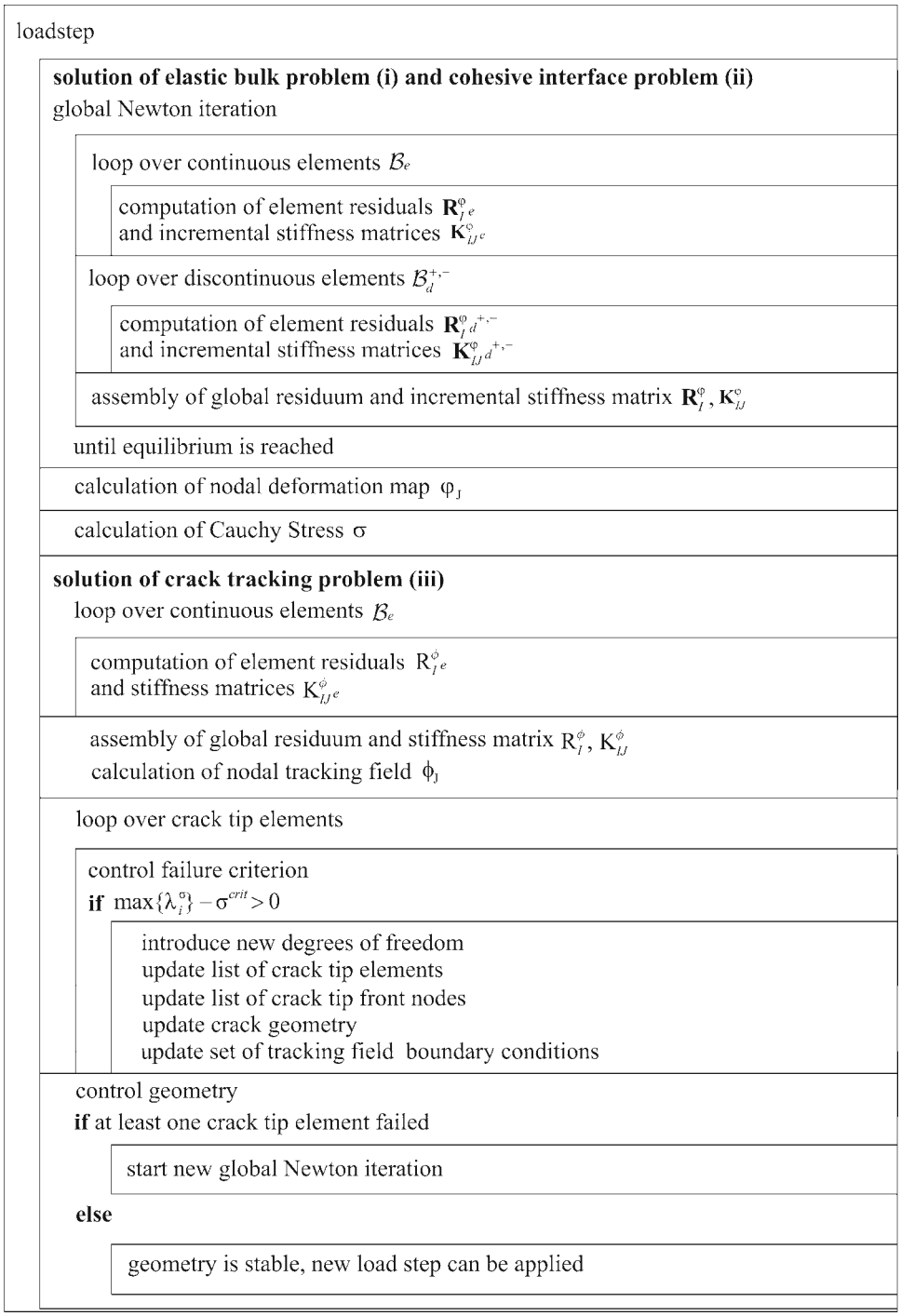

Fig. 4 Algorithmic flowchart of finite element based failure algorithm

further subdivided into tetrahedral elements, we only determine the volume of each tetrahedron or wedge element in a local element coordinate system and weight the stiffness matrix with the corresponding volume. For the sake of clarity we express this integration for a general function $f(\boldsymbol{X})$ which can be understood as a place holder for the volume parts of $\mathbf{K}^{\varphi}_{IJ}e$ and $\mathbf{R}^{\varphi}_{I}e$. Thereby ξ denote the local element coordinates.

$$\int_{\mathcal{B}^{+,-}_d} f(\boldsymbol{X})\,\mathrm{dV} = \int_{\mathcal{B}^{+}_d} f(\boldsymbol{X})^{+}\,\mathrm{dV} + \int_{\mathcal{B}^{-}_d} f(\boldsymbol{X})^{-}\,\mathrm{dV}$$

$$= \sum_{i=1}^{n^{+}_{gp}} f(\xi_{\mathrm{i}})^{+} \det \boldsymbol{J}(\xi_{\mathrm{i}})^{+} \alpha_{\mathrm{i}} + \sum_{j=1}^{n^{-}_{gp}} f(\xi_j)^{-} \det \boldsymbol{J}(\xi_j)^{-} \alpha_{\mathrm{j}} \tag{13}$$

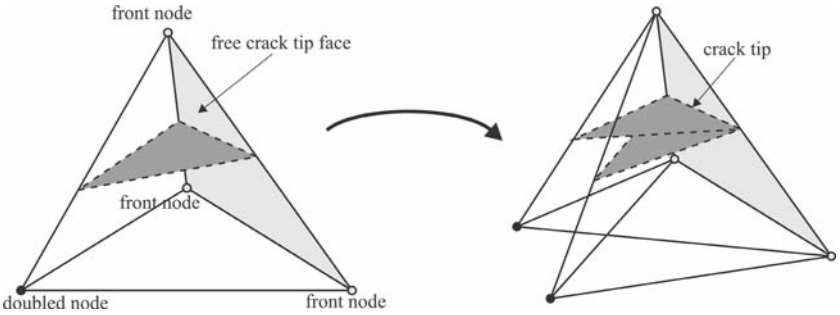

Fig. 5 Local element crack tip with free crack tip face, front nodes and doubled node. *Left* reference configuration. *Right* deformed configuration

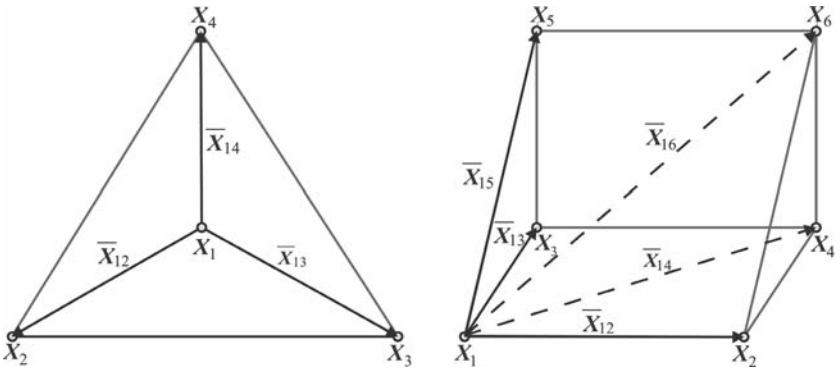

Fig. 6 Numbering convention of local element points and edge vectors. *Left* four-node tetrahedral-element. *Right* six-node wedge-element

Due to the linear approximations of the displacement field we obtain piecewise constant strains and by using one-point gauss integration to determine the particular Jacobians, we obtain the following result.

$$\int_{\mathcal{B}_d^{+,-}} f(\boldsymbol{X})\,\mathrm{dV} = f^{+}\det\boldsymbol{J}(\xi)^{+}\alpha + f^{-}\det\boldsymbol{J}(\xi)^{-}\alpha = f^{+}\,V^{+} + f^{-}\,V^{-} \tag{14}$$

Thereby V^+ and V^- denote the volume of the tetrahedral or wedge part on each side of the discontinuity surface, compare Fig. 6. These volumes can be computed straightforwardly in terms of the intersection points with the help of the following equations.

$$\begin{aligned} \mathrm{V_{tet}} &= \frac{1}{6}[\overline{\boldsymbol{X}}_{12}\times\overline{\boldsymbol{X}}_{13}]\cdot\overline{\boldsymbol{X}}_{14} \\ \mathrm{V_{wedge}} &= \frac{1}{6}[\overline{\boldsymbol{X}}_{13}\times\overline{\boldsymbol{X}}_{15}+\overline{\boldsymbol{X}}_{14}\times\overline{\boldsymbol{X}}_{13} \\ &\quad +\overline{\boldsymbol{X}}_{12}\times\overline{\boldsymbol{X}}_{14}]\cdot\overline{\boldsymbol{X}}_{16} \end{aligned} \tag{15}$$

Concluding this implementation aspect, we describe the numerical integration over the crack surface parts $\mathrm{d}\overline{\mathrm{A}}$. As mentioned above, the crack surface forms either a triangle or a quadrilateral defined by the intersection points. This facilitates the numerical integration over the crack surface. We perform a standard two dimensional Gauss integration scheme with at least three integration points for triangular and four integration points for quadrilateral crack surfaces.

3.5 Load and boundary conditions

A crucial issue that has been neglected in the literature is the physical interpretation, the understanding, and the appropriate definition of load and boundary conditions for the onset of cracking. Therefore, we give an overview of possible boundary conditions and we recapitulate these definitions with regard to the numerical examples. It is important to keep in mind that the set of boundary nodes $\partial\mathcal{B}_\phi$ for the linear crack tracking problem increases during ongoing crack propagation to ensure the kinematical continuity of the crack tracking problem. This implies that we have to update the set of boundary conditions continuously during runtime as mentioned in Fig. 4. To this end, we add the actual ϕ values of the considered cracked elements at loading step n to the set of fixed boundary conditions $\partial\mathcal{B}_\phi$ at loading step n+1 and solve the linear system of equations for the free ϕ values, symbolized in the following static condensation scheme with index f.

$$\begin{bmatrix} \mathrm{K}_{\phi\phi}^{\mathrm{n+1}} & K_{\phi\mathrm{f}}^{\mathrm{n+1}} \\ \mathrm{K}_{\mathrm{f}\phi}^{\mathrm{n+1}} & K_{\mathrm{ff}}^{\mathrm{n+1}} \end{bmatrix} \begin{bmatrix} \phi_{\phi}^{\mathrm{n}} \\ \phi_{\mathrm{f}}^{\mathrm{n+1}} \end{bmatrix} = \begin{bmatrix} \mathrm{R}_{\phi}^{\mathrm{n+1}} \\ \mathrm{R}_{\mathrm{f}}^{\mathrm{n+1}} \end{bmatrix} \tag{16}$$

With this procedure, we ensure that the crack transfer between the discrete finite element remains continuous. This implies that the actual crack surface is frozen during ongoing crack propagation. Next, we have to define either the initial boundary conditions or the so-called root elements to determine the set of onset conditions during a running crack simulation. In the present formulation we only use a set of initial boundary conditions since we validated our algorithm

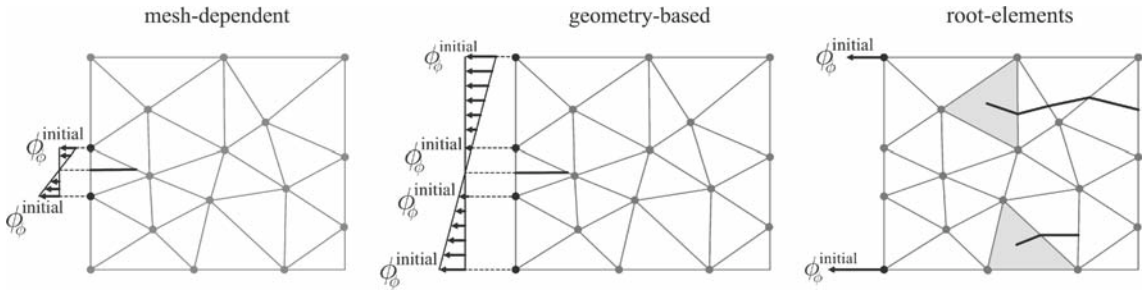

Fig. 7 Illustration of different crack onset boundary conditions for the global crack tracking problem

in terms of experiments and benchmarks from the literature and we therefore wanted to restrict the possible number of cracks. However, the incorporation of root elements which allow for an arbitrary number of cracks is straightforward, see, e.g., [3,5,63]. In the sequel we categorize the choice of boundary conditions first addressing the initial boundary conditions and focusing on the onset boundary conditions or so-called root elements.

Mesh-dependent initial boundary conditions

The simplest way to define initial boundary conditions is to fix the ϕ values for a crack tip or the notch as illustrated in Fig. 7. In the case of tetrahedral elements, we thus have fixed at least three element nodes, which are in fact enough to ensure that the linear equation system for the global tracking field is solvable. Note that only the slope of the chosen start values is important. If, e.g., the crack should start in the middle of the element, the chosen start values will be set to $\phi_\phi^{\text{initial}} = \pm\alpha$ where α can be chosen arbitrarily. Theoretically, the crack surface value $\phi = \text{const.}$ that characterizes the crack surface can also be chosen arbitrarily, although we typically suggest $\phi = \text{const.} = 0$. Mesh dependent boundary conditions are extremely useful in case of a single crack and with relatively simple meshes as we will illustrate in the numerical example of the L-shaped panel. The fundamental drawback of mesh dependent boundary conditions is that they have to be adapted for each discretization to ensure that crack onsets are equal for all computations.

Geometry-based initial boundary conditions

To avoid the modifications of the boundary conditions for each mesh, we recommend to define the boundary conditions based on the geometry, see again Fig. 7. This allows us to pre-determine and fix the initial values for the entire geometry. Moreover, this procedure ensures that both the onset of crack and the boundary conditions are equal for all different meshes. The first situation is extremely helpful for more demanding geometries, which will be illustrated by the numerical simulation of a pull-out test. The latter issue is crucial to ensure symmetric initial boundary conditions in the case of more than one crack, which we will document by the numerical example of the Nooru-Mohamed test. Similar to the previous category, we can choose the crack surface describing $\phi = \text{const.}$ value arbitrarily.

Root-element onset boundary conditions

Finally, a promising technique is the determination of crack onsets during crack propagation, see, e.g., [3,5]. This strategy allows us to describe multiple crack propagation without having to pre-define boundary conditions, compare again Fig. 7. At detection of failure, we first check the minimal and maximal computed values of the crack tracking ϕ field for the considered element. Next, we check if a root element exists within this range. If so, we take the stored $\phi = \text{const.}$ value for this root element. Otherwise we introduce a new root element and assign the $\phi = \text{const.}$ value to the element center point. This procedure uniquely ensures C^0 continuity, for all possible crack surfaces and is more general than the one reported by [63], where root elements are predefined. Although this approach seems to be the most general one, an essential drawback remains: By using finite elements as the root of crack propagation, it is obviously that the number of cracks will inherently depend on the number of elements. This disadvantage, however, can only be avoided by describing the complete crack surface independent of the finite element mesh.

3.6 Visualization of discontinuous failure

To complete the description of the finite element simulation tool, we discuss the visualization of three-dimensional discontinuity surfaces. Although a bit cumbersome, this visualization is straightforward. However, it is an absolutely integral part of the simulation tool that allows us to evaluate the features of the crack path tracking algorithm. For the sake of clarity, we restrict ourselves to the visualization of discontinuous linear tetrahedral elements. Recall that within the presented approach, a discontinuous element is realized by

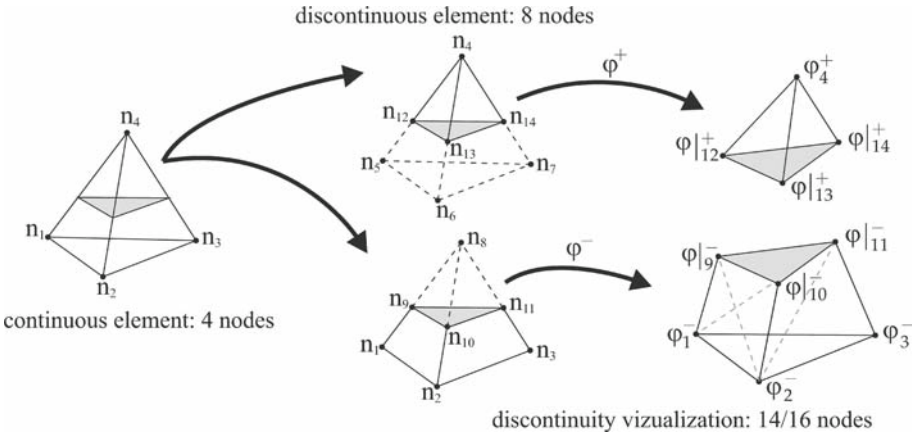

Fig. 8 Additional nodes and modified displacement interpolation for discontinuity visualization procedure

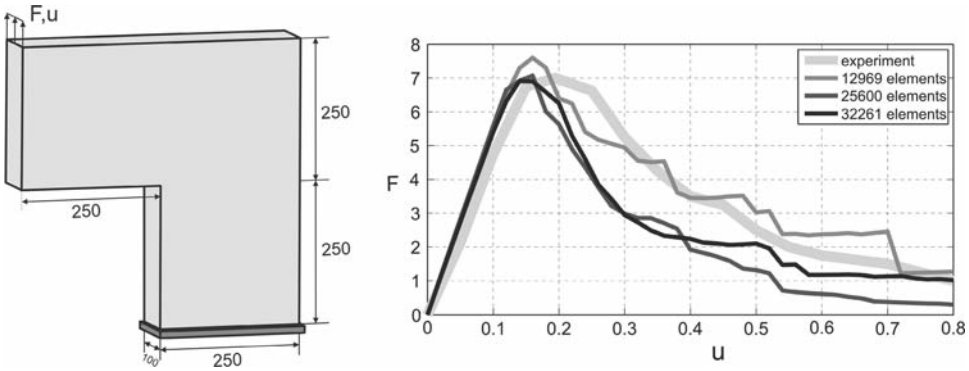

Fig. 9 *Left* geometrical dimensions (mm) and loading, *Right* load displacement relationship F(kN) versus u (mm)

doubling all degrees of freedom, i.e., we double the entire continuous element, compare Fig. 8. Next, two deformation maps are approximated independently with the now available eight element nodes. To post process the discontinuity, six or eight additional nodes have to be introduced. The number of nodes depends on the particular crack surface shape, i.e., three pairs of nodes are required for a triangular crack surface whereas four pairs of nodes are required for a quadrilateral crack surface. A pair of nodes has to be introduced for each edge cut by the discontinuity. Obviously, this pair of nodes has the same referential positions. However, since we allow for finite deformations, these nodes are mapped to different positions in the current configuration, compare also Fig. 8.

Finally, we give a comment on the stress visualization. It is obvious that due to the applied numerical integration, the stresses are only available at the corresponding integration points. Accordingly, we apply a standard projection of the integration point values onto the nodes by virtue of the element shape-functions. In doing so, we obtain the stresses for the eight nodal values of the discontinuous elements. The individual stress contributions at the node are processed similarly to the displacements to obtain the stress values for the additional nodes required for the visualization.

4 Numerical examples

We present three numerical examples illustrating the potential of the proposed algorithmic tool set. These examples have been tailored to address the following aims: (i) to validate the proposed algorithm in terms of well-documented experimental benchmark problems, (ii) to compare the algorithmic performance in relation to existing algorithms in the literature, and (iii) to illustrate the choice of boundary conditions for the additional field of the global tracking problem.

4.1 L-shaped panel

The first example is a concrete L-shaped panel. The geometry and the loading conditions can be found in Fig. 9 left. This geometry was elaborated experimentally by Winkler et al. [64,65]. Comparative discrete failure simulations of this benchmark problem can be found, e.g., in [59]. However, their analysis is restricted to a two-dimensional setting. The domain has been discretized with three different meshes. One structured mesh with 12969 (8658 ndof) tetrahedral elements and two unstructured meshes with 25600 (18711 ndof) and 32261 (19416 ndof) tetrahedral elements respectively. The chosen material parameters are $E = 25,850 \mathrm{N/mm}^2$,

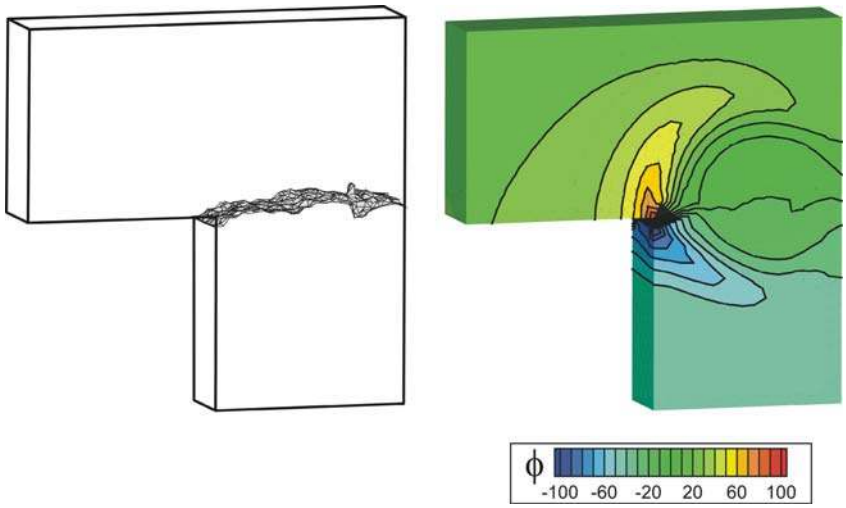

Fig. 10 *Left* potential crack surface, *Right* iso-surfaces for an imposed displacement of $u = 0.8\,\text{mm}$

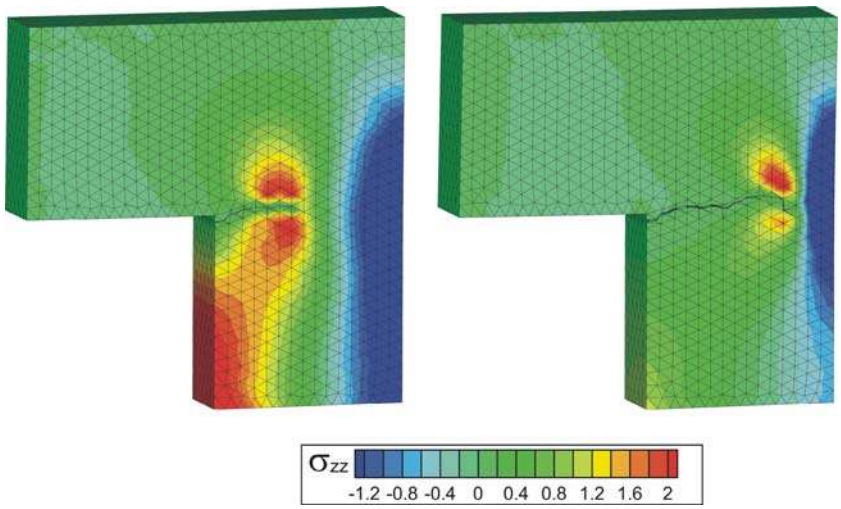

Fig. 11 Cauchy stress (N/mm^2) in loading direction for imposed displacements of $u = 0.2\,\text{mm}$ and $u = 0.4\,\text{mm}$ scaled with factor 20

$\nu = 0.18$, $f_t = 2.7\text{N/mm}^2$, and $G_f = 0.065\text{N/mm}$. The load is applied incrementally through displacement control, i.e., the upper left row of nodes is displaced by $u = 0.02\,\text{mm}$ in 40 load steps each. The corresponding load displacement curves and the reference solution of the experimental investigation are displayed in Fig. 9 right. For the boundary conditions of the global tracking problem we have chosen the mesh dependent case. This implies that we define the onset of crack propagation in the top element of the bottom margin for the discretization with 32261 elements. We have chosen the boundary conditions to ± 100, compare Fig. 10 on the right hand side. Clearly we have to modify the boundary conditions for the other two meshes, to ensure equal initial crack onset conditions for each of the three cases. In detail we fix the value of 100 on the upper side of the element and compute the lower value with regard to the known crack starting position.

The solution is truly mesh independent and in remarkably good agreement with the experimental reference curve, compare Fig. 9. Figure 11 shows the stress distribution plotted on the deformed configuration. The displayed analysis is based on the discretization with 32261 linear tetrahedral elements and shows the results of load steps 10 and 20, i.e., at an applied deformation of $u = 0.2\,\text{mm}$ and $u = 0.4\,\text{mm}$, respectively.

By means of the iso-lines on the outer boundary of the L-shaped panel, Fig. 10 shows how the crack propagates smoothly to the right edge of the specimen as the load is increased. Additionally, Fig. 10 displays the crack surface or rather the zero iso-surface for an imposed displacement of $u = 0.8\,\text{mm}$.

In summary, this example of the cracked L-shaped panel shows that the numerical method is able to capture brittle fracture in a realistic way. The computational simulation matches the experimental findings. The results are truly mesh-independent. For examples with simple geometries such as the L-shaped panel, the first type of boundary conditions for the additional field prove to be straightforward and extremely useful.

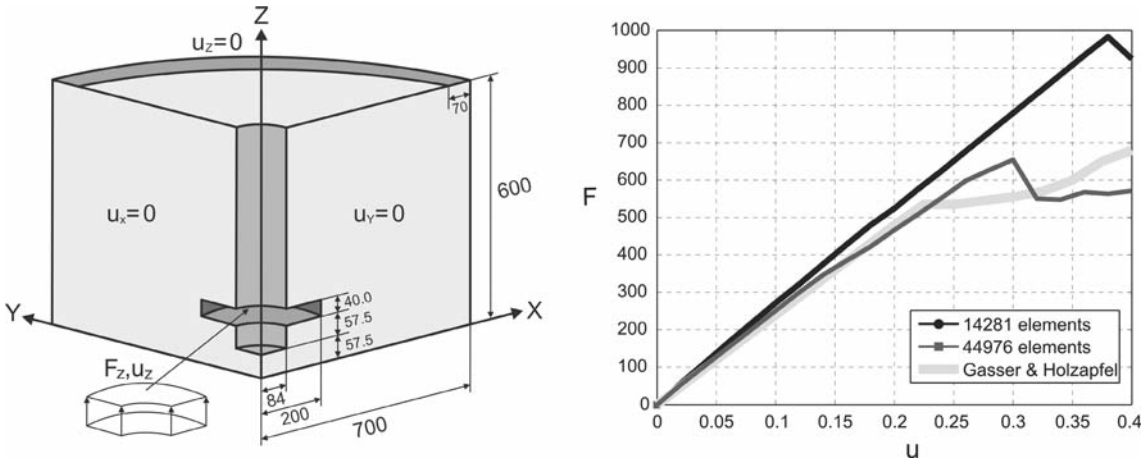

Fig. 12 *Left* geometrical dimensions (mm) and loading, *Right* load displacement relationship F (kN) versus u (mm)

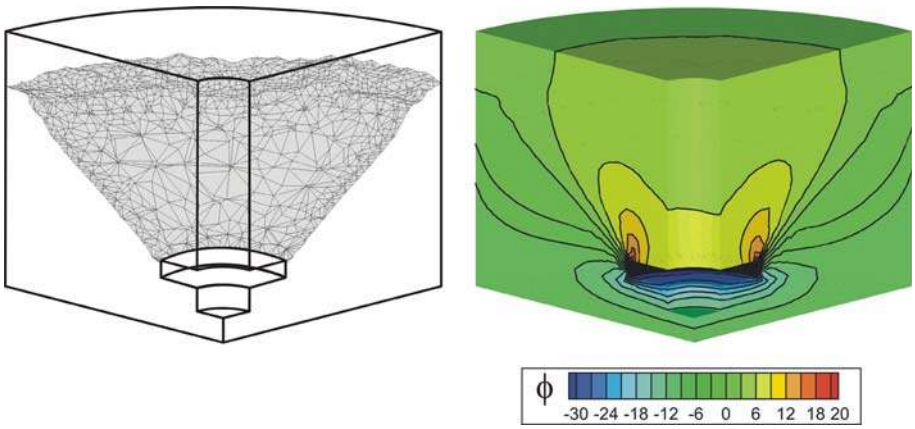

Fig. 13 *Left* potential crack surface, *right* iso-surfaces for an imposed displacement u = 0.6 mm

4.2 Pull-out test

The second example treats the pull-out of a steel anchor embedded in a cylindrical concrete block. The geometrical dimensions of the problem with its loading and boundary conditions are displayed in Fig. 12 for one quarter of the block. The geometry as well as the following material parameters $E = 30,000\,\mathrm{N/mm^2}$, $\nu = 0.2$, $f_t = 3\,\mathrm{N/mm^2}$, $G_f = 0.106\,\mathrm{N/mm}$ are chosen similar to those in [4,35,60]. Here, the steel anchor is not explicitly modeled. Instead an incremental vertical displacement of $u = 0.01\,\mathrm{mm}$ is imposed in 60 load-steps, until the final displacement of $u = 0.4\,\mathrm{mm}$ is reached. Note that for a regular mesh, the considered problem is axis-symmetric and can as well-treated with a computation especially for axis-symmetric conditions, compare, e.g., [66,67]. Since the focus of this work is the investigation of our three-dimensional algorithm, we explore the pull out test in a fully three dimensional setting. Because of the rather complicated geometry, we apply the second category of defined boundary conditions. Accordingly, we predefine the initial boundary conditions for the entire area which is in contact with the surface of the steel disc. In detail we set the nodal values of the upper edge of this part to 20 whereas the bottom nodal values of the bottom are set to −30. Additionally we compute all nodal values of the intermediate nodes keeping in mind the favored crack onset. Hence, we can ensure that the crack onset and the boundary conditions, are equal for various different meshes.

To explore mesh-independency of our algorithm, we use two unstructured meshes containing of 14281 (9525 ndof) and 44976 (28458 ndof) elements, respectively.

The corresponding load displacement curves are shown in Fig. 12, where the two computations are compared with the results from the literature, see, e.g., [4]. The reaction force is linear until the maxim load is reached. Afterwards, we observe a short decrease of the load for both meshes until a re-increase can be noticed for the finer mesh. This is due to the fact, that the crack starts from the onset at the steel disc and propagates further to the inside edge of the counterpressure ring, compare Fig. 13, where the iso-lines and the detailed zero iso-surface are depicted. Because of the tensile failure criterion, the maximal reaction force prior the crack runs below the counterpressure ring.

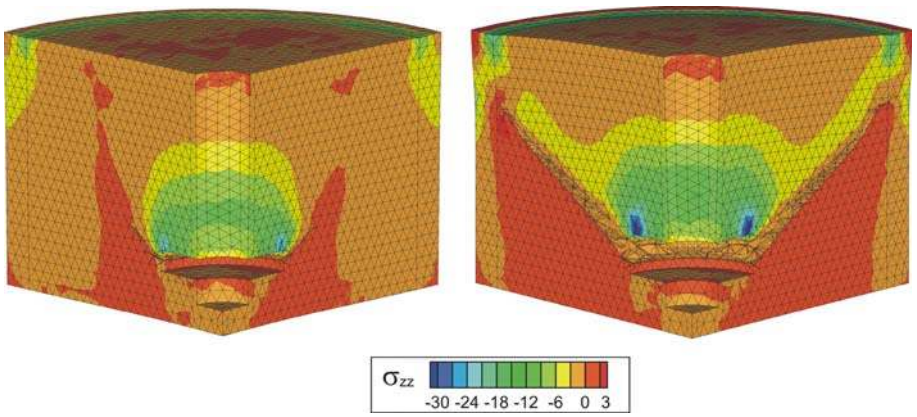

Fig. 14 Cauchy stress (N/mm^2) in loading direction for imposed displacements $u = 0.25\,mm$ and $u = 0.6\,mm$ scaled with factor 100

The mentioned re-increase occurs due to the fact that the failure behavior switches from tensile/shear to compression/shear behavior which cannot yet be captured with the presented numerical framework. It is obvious that the first mesh is too coarse to capture the failure behavior precisely: The peak load is over-estimated and accordingly, the re-increasing of the load occurs later. The reaction force of the finer mesh, however, shows the same linear slope as in the comparison literature and the load exhibits the characteristic re-increase reported in [4]. Finally, Fig. 14 shows the stress distribution plotted on the deformed configuration. The displayed analysis is based on the discretization with 44976 linear tetrahedral elements and shows the results of load steps 25 and 60, i.e., at an applied deformation of $u = 0.25\,mm$ and $u = 0.6\,mm$, respectively.

In summary this example of the pull-out-test documents that the proposed algorithmic tool set is able to capture brittle failure in more complex geometries. The results of the simulation agree nicely with the results documented in the literature. For complex geometries such as the pull-out-test, however, the second type of boundary conditions seems to be the appropriate choice to capture the documented failure behavior appropriately.

4.3 Nooru-Mohamed test

The third example is a tension-shear test which has been experimentally performed by Nooru-Mohamed [68]. From the documented experiments we choose the specimen with size $200 \times 200 \times 50\,mm$ and loading protocol 4b as illustrated in Fig. 15. In this test, a double notched specimen is first loaded by a shear force $Fs = 10\,kN$ on the upper left frame b, whereas frame a is fixed in loading direction. The applied shear force leads to a relative shear displacement δ_s. Afterwards, the specimen is loaded by an imposed tensile displacement u_t on the upper left frame while keeping the shear force constant at $F_s = 10\,kN$. The imposed tensile displacement induces a tensile load F_t whereas, for the results, this tensile load is plotted versus the depicted relative displacement δ_t, see Fig. 15. It is obvious, that keeping the shear load F_s constant leads to a further increase in shear displacement during tensile loading. Due to this loading protocol, the principal stresses rotate during loading and result in two curvilinear cracks starting from the opposite notches. This example is thus an excellent test platform for our algorithm to simulate more than one crack.

For the presented simulations we use two unstructured meshes consisting of 14681 (9303 ndof) and 35176 (21021 ndof) elements, respectively. The material parameters are chosen as follows $E = 30{,}000\,N/mm^2$, $\nu = 0.2$, $f_t = 3\,N/mm^2$ and $G_f = 0.11N/m$, similar to those in the literature [30,68]. Comparative discrete failure simulations of this benchmark problem can be found, e.g., in [3,30,69]. To ensure the mentioned loading protocol, we couple the degrees of freedom in the shear direction to apply the shear force. Then, we use 320 displacement controlled loadsteps of $u_t = 0.001\,mm$. This example is well suited to demonstrate the importance of boundary conditions for the crack tracking problem in the context of defining symmetric initial conditions. That means, if we want to achieve a symmetric solution for the crack tracking problem and accordingly for the mechanical problem, we have to begin with a symmetric setup. Accordingly, the mesh-dependent boundary conditions previously used in the literature are not useful. We thus choose to apply the initial boundary conditions on the geometry. In detail, we predefine the particular areas of the notches starting with -50 on the outside and ending with $+5$ on the inner side of the particular area introducing symmetric initial boundary conditions as displayed in Fig. 16.

The onset of crack propagation occurs on the notches as imposed. Thereby, the cracks will propagate under mode II 45° as long as the shear load is applied. Afterwards, with increasing tensile loading, the cracks rotate as mentioned before, compare, Fig. 16, in which both the iso-lines and the zero-iso-surface are displayed. The crack path is in remarkably good qualitative agreement with the crack pattern of the experiments, [68]. The reaction force is mesh independent but the peak load is slightly overestimated compared to the

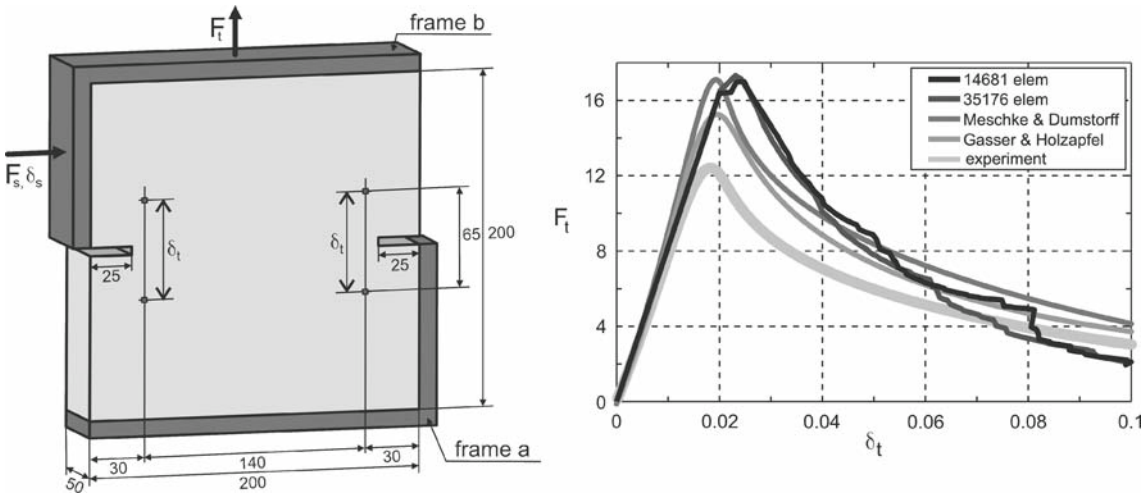

Fig. 15 *Left* geometrical dimensions (mm) and loading. *Right* load displacement relationship F_t(kN) versus δ_t(mm)

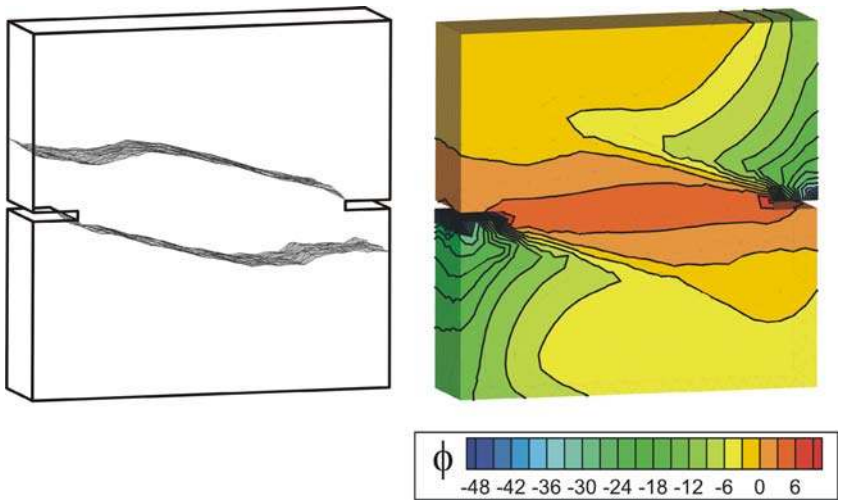

Fig. 16 *Left* potential crack surface. *Right* iso-surfaces for an imposed displacement $u_t = 0.28$ mm ($\delta_t = 0.0922$)

experiment. However, this is also the case for the comparison with numerical analyses of Meschke and Dumstorff in two dimensions and Gasser and Holzapfel in three dimensions whereas the latter simulation is in closest agreement with the experiments. The reason for the over-estimation of the peak can be explained by the following considerations: First, the fracture energy $G_f = 0.11$ N/m is not experimentally determined in the original work [68]. Its value is only estimated for the numerical simulations in the corresponding literature. We assume that the fracture energy could be overestimated itself. Second, the used exponential cohesive model could have over-estimated the peak load because only tractions normal to the interface are considered. This is a first approach reasonable for tensile-dominated failure. For the present mixed-mode example, which is dominated by shear failure especially at the onset of cracking, we should also account for the tangential tractions. Third, we have used relatively uniform meshes without mesh-refinement at the notches which could also be a factor for the overestimated peak load.

Finally, Fig. 17 shows the principal stress distribution of the deformed configuration. The displayed analysis is based on the discretization with 35176 elements and shows the results of imposed displacements of $u_t = 0.025$ mm ($\delta_t = 0.0247$) and $u_t = 0.28$ mm ($\delta_t = 0.0922$) whereby the displacement is scaled with factor 25.

In summary, the simulation of the Nooru-Mohamed test has demonstrated the potential of the proposed tool set to model multiple curved cracks. The results of the computational simulation agree qualitatively and quantitatively with experimental findings as well as with computational results achieved with alternative simulation tools.

5 Discussion

We have illustrated the computational design of a modular algorithmic tool for modeling brittle fracture within the finite element setting. The suggested approach combines different

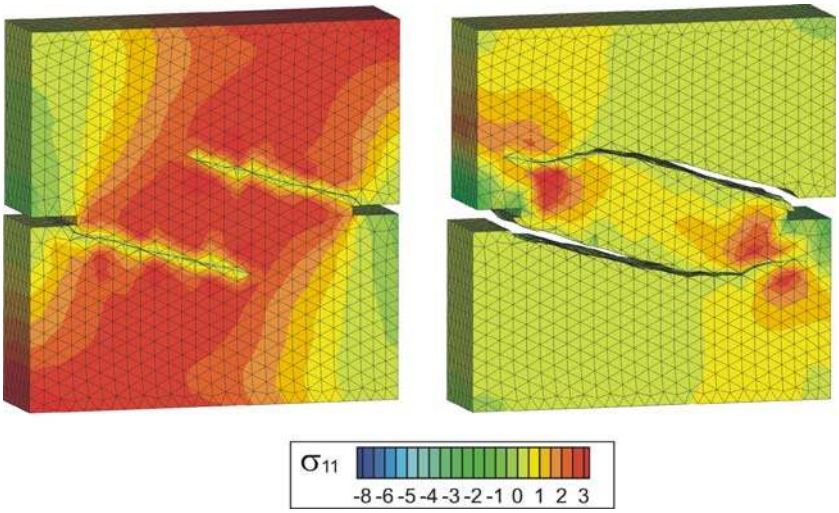

Fig. 17 Principal Cauchy stress (N/mm^2) for imposed displacements $u_t = 0.025$ mm ($\delta_t = 0.0247$) and $u_t = 0.28$ mm ($\delta_t = 0.0922$) scaled with factor 25

recently proposed approaches to tackle the non-unique problem of crack propagation in three dimensions. The resulting algorithm has been demonstrated to be able to characterize the formation of failure surfaces in typical engineering applications. The computational simulations have been validated by means of experiments and simulations with alternative algorithmic tools documented in the literature. The proposed framework is essentially composed of three ingredients: (i) the elastic bulk problem, (ii) the cohesive interface problem, and (iii) the crack tracking problem. Due to its modular nature, the proposed tool shows a great development potential. It can be generalized to other kinds of materials or loading scenarios by simply modifying the constitutive equations for the bulk material. Ductile fracture and time dependent problems can be treated straightforwardly with only small algorithmic modifications. In particular, high impact failure and explosion of concrete structures can be simulated by adding transient terms. The prediction of safety and reliability of concrete buildings, bridges, storage containers, and other engineering structures constitutes another potential field of application of the proposed approach. As failure is only represented through the interface, the suggested framework relies on only very few material parameters and the examples have demonstrated that their fit is straightforward. A possible generalization would be to include history variables in the cohesive law, e.g., similar to a damage or plasticity type formulation that is able to account for loading / unloading processes. Cohesive laws seem to be ideally suited to incorporate irreversible damage processes in a phenomenological sense.

In previous studies, we have extensively elaborated the crack tracking problem that characterizes the crack kinematics. Based on systematic comparisons, we have decided to focus on the global tracking algorithm that couples the crack kinematics with the chosen crack propagation criterion. Since this approach is relatively novel, it still faces a number of technical difficulties which we have tried to address in this manuscript. Similar to most multifield problems which are not directly linked to first principles, it is not straightforward to define the boundary conditions for the additional field. We have classified the possible types of boundary conditions for the crack tracking problem. For each category, we have identified different scenarios for which they are particularly useful. The proposed guidelines to choose the appropriate boundary conditions have been verified by three numerical examples of different complexity.

We are aware that the extension of the global tracking algorithm to more sophisticated crack propagation laws, necessary to treat more complex failure mechanisms, is not as straightforward as the extension of the bulk and the cohesive interface problem. Nevertheless, we believe that the coupling of a continuous level set function with the here suggested failure criterion similar to the global tracking scheme is also possible for other crack propagation criteria. We are currently exploring the potential of the proposed algorithm of generalizations along these lines.

Acknowledgments This work is part at the research project carried out within the DFG graduate school 814 “Engineering materials on different scales”. We would kindly like to acknowledge its support through the German National science foundation.

References

1. Geers MGD, de Borst R, Peerlings RHJ (2000) Damage and crack modeling in single-edge and double-edge notched concrete beams. Eng Fract Mech 65(2–3):247–261
2. Ruiz G, Ortiz M, Pandolfi A (2000) Three-dimensional finite-element simulation of the dynamic Brazilian tests on concrete cylinders. Int J Numer Meth Eng 48(7):963–994

3. Oliver J, Huespe AE, Samaniego E, Chaves EVW (2004) Continuum approach to the numerical simulation of material failure in concrete. Int J Numer Anal Meth Geomech 28(7–8):609–632
4. Gasser TC, Holzapfel GA (2005) Modeling 3D crack propagation in unreinforced concrete using PUFEM. Comput Methods Appl Mech Eng 194(25–26):2859–2896
5. Feist C, Hofstetter G (2006) An embedded strong discontinuity model for cracking of plain concrete. Comput Methods Appl Mech Eng 195(52):7115–7138
6. Grassl P, Jirasek M (2006) Plastic model with non-local damage applied to concrete. Int J Numer Anal Meth Geomech 30(1):71–90
7. Gasser TC, Holzapfel GA (2006) 3D Crack propagation in unreinforced concrete. A two-step algorithm for tracking 3D crack paths. Comput Methods Appl Mech Eng 195(37–40):5198–5219
8. Sancho JM, Planas J, Fathy AM, Galvez JC, Cendon DA (2007) Three-dimensional simulation of concrete fracture using embedded crack elements without enforcing crack path continuity. Int J Numer Anal Meth Geomech 31(2):173–187
9. Sancho JM, Planas J, Cendon DA, Reyes E, Galvez JC (2007) An embedded crack model for finite element analysis of concrete fracture. Eng Fract Mech 74(1–2):75–86
10. Feist C, Hofstetter G (2007) Crack propagation in plain concrete. Part I: Experimental investigation—the PCT3D test. Comput Concrete 4(1):49–66
11. Gasser TC (2007) Validation of 3D crack propagation in plain concrete. Part II: Computational modeling and predictions of the PCT3D test. Comput Concrete 4(1):67–82
12. Needleman A (1990) An analysis of decohesion along an imperfect interface. Int J Fract 42(1):21–40
13. Xu XP, Needleman A (1994) Numerical simulations of fast crack growth in brittle solids. J Mech Phys Solids 42(9):1397–1434
14. Simone A (2004) Partition of unity-based discontinuous elements for interface phenomena: computational issues. Commun Numer Meth Eng 20(6):465–478
15. Utzinger J, Menzel A, Steinmann P, Benallal A (2008) Aspects of bifurcation in an isotropic elastic continuum with orthotropic inelastic interface. Eur J Mech, in press
16. Swenson DV, Ingraffea AR (1988) Modeling mixed-mode dynamic crack propagation using finite elements: theory and applications. Comput Mech 3:381–397
17. Askes H, Sluys LJ, de Jong BBC (2001) Remeshing techniques for r-adaptive and combined h/r-adaptive analysis with application to 2D/3D crack propagation. Struct Eng Mech 12(5):475–490
18. Dvorkin EN, Cuitino AM, Gioia G (1990) Finite-elements with displacement interpolated embedded localization lines insensitive to meshsize and distortions. Int J Numer Meth Eng 30(3): 541–564
19. Simo JC, Armero F, Taylor RL (1993) Improved versions of assumed enhanced strain tri-linear elements for 3D-finite deformation problems. Comput Methods Appl Mech Eng 110(3–4):359–386
20. Armero F, Garikipati K (1996) An analysis of strong discontinuities in multiplicative finite strain plasticity and their relation with the numerical simulation of strain localization in solids. Int J Solids Struct 33(20–22):2863–2885
21. Bolzon G, Corigliano A (2000) Finite elements with embedded displacement discontinuity: a generalized variable formulation. Int J Numer Meth Eng 49(10):1227–1266
22. de Borst R, Wells GN, Sluys LJ (2001) Some observations on embedded discontinuity models. Eng Comput 18(1/2):241–254
23. Oliver J, Huespe AE, Samaniego E (2003) A study on finite elements capturing strong discontinuities. Int J Numer Meth Eng 56(14):2135–2161
24. Schröder J, Löblein J (2005) A geometric nonlinear triangular finite element with an embedded discontinuity for the simulation of quasi-brittle fracture. Comput Mech 36(2):139–157
25. Dolbow J, Moës N, Belytschko T (2000) Discontinuous enrichment in finite elements with a partition of unity method. Finite Elem Anal Design 36(3–4):235–260
26. Belytschko T, Moës N, Usui S, Parimi C (2001) Arbitrary discontinuities in finite elements. Int J Numer Method Eng 50(4):993–1013
27. Bordas S, Moran B (2006) Enriched finite elements and level sets for damage tolerance assessment of complex structures. Eng Fract Mech 73(9):1176–1201
28. Mosler J (2006) Modeling strong discontinuities at finite strains—a novel numerical implementation. Comput Methods Appl Mech Eng 195(33–36):4396–4419
29. Fagerström M, Larsson R (2006) Theory and numerics for finite deformation fracture modelling using strong discontinuities. Int J Numer Meth Eng 66(6):911–948
30. Meschke G, Dumstorff P (2007) Energy-based modeling of cohesive and cohesionless cracks via X-FEM. Comput Methods Appl Mech Eng 196(21–24):2338–2357
31. Sukumar N, Moës N, Moran B, Belytschko T (2000) Extended finite element method for three-dimensional crack modeling. Int J Numer Method Eng 48(11):1549–1570
32. Moës N, Gravouil A, Belytschko T (2002) Non-planar 3D crack growth by the extended finite element and level sets—Part I: Mechanical model. Int J Numer Method Eng 53(11):2549–2568
33. Gravouil A, Moës N, Belytschko T (2002) Non-planar 3D crack growth by the extended finite element and level sets—Part II: level set update. Int J Numer Meth Eng 53(11):2569–2586
34. Mosler J, Meschke G (2003) 3D modelling of strong discontinuities in elastoplastic solids: fixed and rotating localization formulations. Int J Numer Method Eng 57(11):1553–1576
35. Areias PMA, Belytschko T (2005) Analysis of three-dimensional crack initiation and propagation using the extended finite element method. Int J Numer Method Eng 63(5):760–788
36. Pandolfi A, Ortiz M (2007) An efficient adaptive procedure for three-dimensional fragmentation simulations. Eng Comput 18(2):148–159
37. Hansbo A, Hansbo P (2004) A finite element method for the simulation of strong and weak discontinuities in solid mechanics. Comput Methods Appl Mech Eng 193(33–35):3532–3540
38. Hansbo A, Hansbo P, Larson MG (2003) A finite element method on composite grids based on Nitsche's method. ESAIM Math Modell Numer Anal 37(3):495–514
39. Areias PMA, Belytschko T (2006) A comment on the article "A finite element method for the simulation of strong and weak discontinuities in solid mechanics" By Hansbo A, Hansbo P [Comput Methods Appl Mech Eng (2004) 193:3523–3540]. Comput Methods Appl Mech Eng 195(9–12):1275–1276
40. Mergheim J, Kuhl E, Steinmann P (2004) A hybrid discontinuous Galerkin/interface method for the computational modelling of failure. Commun Numer Meth Eng 20(7):511–519
41. Mergheim J, Kuhl E, Steinmann P (2005) A finite element method for the computational modelling of cohesive cracks. Int J Numer Meth Eng 63(2):276–289
42. Kuhl E, Jäger P, Mergheim J, Steinmann P (2006) On the application of Hansbo's method for interface problems. In: Combescure A, de Borst R, Belytschko T (eds) Proceedings of the IUTAM symposium on discretization methods for evolving discontinuities. Springer, Lyon
43. Mergheim J, Kuhl E, Steinmann P (2007) Towards the algorithmic treatment of 3D strong discontinuities. Commun Numer Meth Eng 23(2):97–108
44. Rabczuk T, Bordas S, Zi G (2006) A three dimensional meshfree method for continuous multiple-crack initiation, propagation and junction in statics and dynamics. Comput Mech 40(3):473–495

45. Rabczuk T, Belytschko T (2007) A three dimensional large deformation meshfree method for arbitrary evolving cracks. Comput Methods Appl Mech Eng 196(29–30):2777–2799
46. Dugdale DS (1960) Yielding of steel sheets containing slits. J Mech Phys Solids 8(2):100–104
47. Barrenblatt GI (1962) The mathematical theory of equilibrium cracks in brittle fracture. Adv Appl Mech 7:55–129
48. Hillerborg A, Modeer M, Petersson PE (1976) Analysis of crack formation and crack growth by means of fracture mechanics and finite elements. Cement Concrete Res 6:773–782
49. Hillerborg A (1990) Applications of the fictitious crack model to different types of materials. Int J Fract 51(2):95–102
50. Ortiz M, Pandolfi A (1999) Finite-Deformation irreversible cohesive elements for three-dimensional crack propagation analysis. Int J Numer Meth Eng 44(9):1267–1282
51. Wells GN, Sluys LJ (2001) A new method for the modelling of cohesive cracks using finite elements. Int J Numer Meth Eng 50(12):2667–2682
52. de Borst R (2003) Numerical aspects of cohesive-zone models. Eng Fract Mech 70(14):1743–1757
53. Remmers JJC, de Borst R, Needleman A (2003) A cohesive segments method for the simulation of crack growth. Comput Mech 31(1–2):69–77
54. de Borst R, Guiti'errez MA, Wells GN, Remmers JC, Askes H (2004) Cohesive-zone models, higher-order continuum theories and reliability methods for computational failure analysis. Int J Numer Meth Eng 60(1):289–315
55. Areias PMA, Rabczuk T (2007) Quasi-static crack propagation in plane and plate structures using set-valued traction separation laws. Int J Numer Meth Eng, published online
56. Oliver J, Huespe AE (2002) On strategies for tracking strong discontinuities in computational failure mechanics. In: Mang HA, Rammersdorfer FG, Erberhardsteiner J (eds) Proceedings of the fifth world congress on computational mechanics (WCCM V). Vienna, Austria
57. Chaves EWV (2006) Tracking 3D crack path. In: Proceeding of the international conference on mathematical and statistical modeling in honor of Enrique Castillo. ICMSM, Ciudad Real, Spain
58. Cervera M, Chiumenti M (2006) Mesh objective tensile cracking via a local continuum damage model and a crack tracking technique. Comput Methods Appl Mech Eng 196(1–3):304–320
59. Dumstorff P, Meschke G (2007) Crack propagation criteria in the framework of X-FEM-based structural analyses. Int J Numer Anal Meth Geomech 31(2):239–259
60. Feist C, Hofstetter G (2007) Three-dimensional fracture simulations based on the SDA. Int J Numer Anal Meth Geomech 31(2):189–212
61. Jäger P, Steinmann P, Kuhl E (2008) On local tracking algorithms for the simulation of three-dimensional discontinuities. Comput Mech 42(3):395–406
62. Jäger P, Steinmann P, Kuhl E (2008) Modeling three-dimensional crack propagation—a comparison of crack path tracking strategies. Int J Numer Meth Eng 76(9):1328–1352
63. Jäger P, Schmalholz SM, Schmied DW, Kuhl E (2007) Brittle fracture during folding of rocks—a finite element study. Philos Mag 88(28–29):3245–3263
64. Winkler BJ, Hofstetter G, Niederwanger G (2001) Experimental verification of a constitutive model for concrete cracking. Proc Inst Mech Eng Part L J Mater Des Appl 215(L2):75–86
65. Winkler BJ (2001) Traglastuntersuchungen von unbewehrten und bewehrten Betonstrukturen auf der Grundlage eines objektiven Werkstoffgesetztes für Beton. Ph.D.Thesis, University of Innsbruck, Austria
66. de Borst R (1986) Non-linear analysis of frictional materials. Ph.D.Thesis, Delft university of Technology, Netherlands
67. Elfgren L, Eligehausen R, Rots JG (2001) Anchor bolts in concrete structures: summary of round robin tests and analysis arranged by RILEM TC 90-FMA 'Fracture Mechanics of Concrete. Mater Struct 34(242):451–457
68. Nooru-Mohamed MB (1992) Mixed-mode fracture of concrete an experimental approach. Ph.D.Thesis, Delft university of Technology, Netherlands
69. Gasser TC, Holzapfel GA (2006) 3D Crack propagation in unreinforced concrete. A two step algorithm for tracking 3D crack paths. Comp Methods Appl Mech Eng 195:5198–5219